Optimization of a Microfluidic Mixer for Studying Protein Folding Kinetics

David E. Hertzog,[†,‡] Benjamin Ivorra,[§] Bijan Mohammadi,[§] Olgica Bakajin,[‡] and Juan G. Santiago*,[†]

Department of Mechanical Engineering, Stanford University, Stanford, California 94305, Chemistry and Materials Science, Lawrence Livermore National Laboratory, Livermore, California 94550, and Mathematics and Modeling Institute of Montpellier, Montpellier University, Montpellier, France

We have applied an optimization method in conjunction with numerical simulations to minimize the mixing time of a microfluidic mixer developed for protein folding studies. The optimization method uses a semideterministic algorithm to find the global minimum of the mixing time by varying the mixer geometry and flow conditions. We describe the minimization problem and constraints and give a brief overview of the optimization algorithm. We present results of the optimization, including the optimized geometry and parameter sensitivities, and we demonstrate the improvement in mixing performance with experiments using microfabricated mixers. The dye-quenching experiments of the original and optimized mixer designs show respective mixing times of 7 and 4 μs, a 40% reduction. The new design also provides more uniform mixing across streamlines that enter the mixer. The optimized mixer is the fastest reported continuous flow mixer for protein folding.

Fast events in protein folding often occur on a microsecond time scale.[1,2] Various techniques exist to initiate protein folding including laser temperature jump,[3] pressure jump,[4,5] photochemical initiation,[6] and changing the concentration of a chemical denaturant.[7−10] Changing denaturant concentration is an attractive method because it enables large thermodynamic perturbations on most biomolecular systems.[11] The technique, however, can be difficult to initiate quickly because molecular diffusion of denaturants is typically slow. Stopped-flow mixers can achieve mixing times on the order of 200 μs, while continuous-flow mixers have achieved less than 100-μs mixing times. Brody et al.[12] first proposed hydrodynamic focusing to reduce diffusion distance and limit sample consumption, and this method has been used with SAXS,[13,14] FT-IR,[11,15] and UV detection[11] techniques with mixing times less than 100 μs. Shastry et al.[10] demonstrated 50−μs mixing times with a turbulent flow device, yet required large sample consumption (600 μL/s). With our previous mixer design,[16] a continuous-flow device using hydrodynamic focusing, we achieved mixing times of less than 10 μs and demonstrated feasibility by measuring folding kinetics of a benchmark protein, acyl-CoA binding protein (ACBP).

Faster mixers need to be developed that can capture folding on the order of 1 μs or less in order to bridge the gap between molecular dynamics (MD) simulations and current experimental data. Experimental and theoretical approaches predict that an *N*-residue single domain protein can fold in $N/100$ μs.[17] MD simulations of protein folding will perhaps offer an insight into fast folding kinetics but are currently extremely computationally intensive, requiring roughly 1 month/μs of CPU time[18] even on the fastest supercomputers. Simulating protein folding events to tens of microseconds requires massive distributed computing platforms not widely available to the community, even with implicit solvent models.[19]

Our original mixer design[16] was a microfluidic device that leveraged hydrodynamic focusing to reduce diffusion length

* Corresponding author: (e-mail) juan.santiago@stanford.edu; (phone) 650.723.5689; (fax) 650.723.7657.
† Stanford University.
‡ Lawrence Livermore National Laboratory.
§ Montpellier University.

(1) Roder, H. *Proc. Natl. Acad. Sci. U.S.A.* **2004**, *101*, 1793−1794.
(2) Eaton, W. A.; Munoz, V.; Hagen, S. J.; Jas, G. S.; Lapidus, L. J.; Henry, E. R. *Annu. Rev. Biophys. Biomol. Struct.* **2000**, *29*, 327−359.
(3) Hagen, S. J.; Eaton, W. A. *J. Mol. Biol.* **2000**, *301*, 1037−1045.
(4) Pryse, K. M.; Bruckman, T. G.; Maxfield, B. W.; Elson, E. L. *Biochemistry* **1992**, *31*, 5127−5136.
(5) Jacob, M.; Holtermann, G.; Perl, D.; Reinstein, J.; Schindler, T.; Geeves, M. A.; Schmid, F. X. *Biochemistry* **1999**, *38*, 2882−2891.
(6) Jones, C. M.; Henry, E. R.; Hu, Y.; Chan, C.-K.; Luck, S. D.; Bhuyan, A.; Roder, H.; Hofrichter, J.; Eaton, W. A. *Proc. Natl. Acad. Sci. U.S.A.* **1993**, *90*, 11860−11864.
(7) Chan, C.-K.; Hu, Y.; Takahashi, S.; Rousseau, D. L.; Eaton, W. A. *Proc. Natl. Acad. Sci. U.S.A.* **1997**, *94*, 1779−1784.
(8) Pollack, L.; Tate, M. W.; Darnton, N. C.; Knight, J. B.; Gruner, S. M.; Eaton, W. A.; Austin, R. H. *Proc. Natl. Acad. Sci. U.S.A.* **1999**, *96*, 10115−10117.
(9) Park, S.-H.; Shastry, M. C. R.; Roder, H. *Nat. Struct.l Biol.* **1999**, *6*, 943−947.
(10) Shastry, M. C. R.; Luck, S. D.; Roder, H. *Biophys. J.* **1998**, *74*, 2714−2721.
(11) Pabit, S. A. a. H. S. J. *Proc. Natl. Acad. Sci. U.S.A.* **2002**, *83*, 2872−2878.
(12) Brody, J. P.; Yager, P.; Goldstein, R. E.; Austin, R. H. *Biophys. J.* **1996**, *71*, 3430−3441.
(13) Akiyama, S.; Takahashi, S.; Kimura, T.; Ishimori, K.; Morishima, I.; Nishikawa, Y.; Fujisawa, T. *Proc. Natl. Acad. Sci. U.S.A.* **2002**, *99*, 1329−1334.
(14) Pollack, L.; Tate, M. W.; Finnefrock, A. C.; Kalidas, C.; Trotter, S.; Darnton, N. C.; Lurio, L.; Austin, R. H.; Batt, C. A.; Gruner, S. M.; Mochrie, S. G. J. *Phys. Rev. Lett.* **2001**, *86*, 4962−4965.
(15) Kauffmann, E.; Darnton, N. C.; Austin, R. H.; Batt, C.; Gerwert, K. *Proc. Natl. Acad. Sci. U.S.A.* **2001**, 6646−6649.
(16) Hertzog, D. E.; Michalet, X.; Jager, M.; Kong, X.; Santiago, J. G.; Weiss, S.; Bakajin, O. *Anal. Chem.* **2004**, *76*, 7169−7178.
(17) Kubelka, J.; Hofrichter, J.; Eaton, W. A. *Curr. Opin. Struct. Biol.* **2004**, *14*, 76−88.
(18) Average computation time for a hemoglobin molecule on AMBER is 8.2 ns-10 000 atoms/month/CPU/GHz (amber.scripps.edu/amber8.bench1.html).
(19) Pande, V. S.; Baker, I.; Chapman, J.; Elmer, S. P.; Khaliq, S.; Larson, S. M.; Rhee, Y. M.; Shirts, M. R.; Snow, C. D.; Sorin, E. J.; Zagrovic, B. *Biopolymers* **2003**, *68*, 91−109.

scales. The mixer was optimized with a parametric optimization method in which we independently varied five nondimensional parameters that described the system to study how these parameters affected mixing time. A variety of physical constraints bounded the optimization, including minimum feature sizes set by microfabrication techniques, transition between approximately 2D to 3D flow fields, and microchannel clogging issues. Our previous mixer requires only femtomoles of labeled proteins and gives access to protein conformational changes far from equilibrium at previously inaccessible time scales. We demonstrated protein folding measurements with mixing times of 8 μs. In this paper, we present an optimization of our previous mixer design using the state-of-the-art shape optimization technique described by Mohammadi and Pironneau.[20,21] We present dye-quenching experiments that demonstrate the performance of our newly optimized design and validate the model.

OPTIMIZATION TECHNIQUES

We consider optimizations of mixer shape and flow rate conditions using mixing time as a cost function. We impose on this optimization the constraints of our microfabrication techniques and flow control system. We apply a global minimization method based on the solution of the boundary value problems of the coupled fluid mechanics and convective diffusion of the mixer. The technique is more robust and general than our previous method and allows for nonintuitive designs to emerge. The optimization begins with our previous mixer design and varies the channel shapes and flow rate ratios at the mixer intersection in order to minimize the mixing time. The current and previous mixer architectures were limited to a three-inlet, one-outlet design.

In our previous design, we fixed the exit channel width (a constraint dictated by achievable channel depth) and set the side channels to intersect at 90° from center inlet and exit channel. The center inlet carried denatured (unfolded) protein solution, and the side inlets carried only buffer. In the current optimization,[22] we again restricted geometry to the three-inlet, one-outlet topology but allowed continuous variations of size, shape, and orientation of all channels in the vicinity of the mixing region. This section summarizes the algorithms used to perform this full shape optimization. For more details of this optimization procedure, see Ivorra et al.[22]

State Equations. The mixer flow was analyzed using numerical solutions of the incompressible Navier−Stokes equations and a convective−diffusion equation for the denaturant. A commercial nonlinear solver (Femlab by Comsol Inc., Stockholm, Sweden) was used to iteratively solve the state equations,

$$-\nabla\cdot(\eta(\nabla\bar{u} + (\nabla\bar{u})^{\mathrm{T}})) + \rho(\bar{u}\cdot\nabla)\bar{u} + \nabla p = 0 \qquad (1)$$
$$\nabla\cdot\bar{u} = 0 \qquad (2)$$
$$\nabla\cdot(-D\nabla c + c\bar{u}) = 0 \qquad (3)$$

where η is the dynamic viscosity, $\bar{u}$ is the velocity with components u and v in the x and y directions (axes shown in Figure 1), ρ is
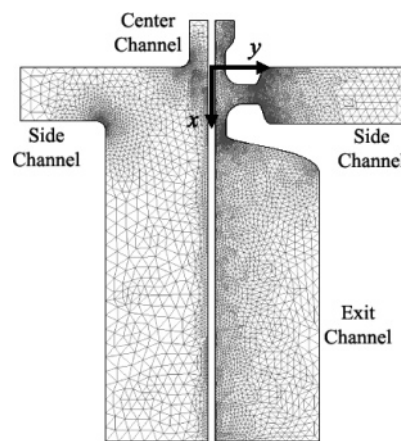

Figure 1. Design of ref 16 (left) and the current shape-optimized geometry (right) with computation grids. The mixers are symmetric about the x-axis so only one symmetric half is modeled to save computation time. The grids are designed to resolve the high-concentration and velocity gradient regions of the focused stream near the intersection and along the centerline. The channels are labeled as center channel (top or north channel), side channels (horizontal or east/west channels), and exit channel (bottom or south channel).

the density, p is the pressure, D is the diffusivity, and c is the concentration of denaturant. Equations 1−3 are subject to the following boundary conditions:

$$\bar{u}(\bar{x}_{\mathrm{w}}) = 0 \qquad (4)$$
$$\nabla c\cdot\hat{n} = 0 \qquad (5)$$

where $\bar{x}_{\mathrm{w}}$ denotes the location of walls and $\hat{n}$ is the wall unit normal vector. Equation 4 accounts for no-slip and no penetration boundary conditions, and eq 5 enforces the condition of zero diffusional flux at the walls.

Semideterministic Algorithm (SDA). Consider a function $J(x)$ with parameters x, taking their values in X, a subset of R^n (n being the size of vector x). Any optimization problem can be seen as finding the value x in the real set X such that J is minimized.[20,21] In compact notation, the minimization of $J: X \rightarrow R$. We will use a new SDA.[23] SDA aims to improve the efficiency of any local minimization algorithm (gradient based, Newton, etc.). Such local algorithms yield solutions determined by local minima except if the initial condition is in the attraction basin of the global optimum.[24] SDA is designed to find an initial condition in the global optimum attraction basin in order to achieve global optimization. Two of us (B.I. and B.M.) have applied the technique with success to various industrial problems including temperature and pollution control in a Bunsen flame,[25] shape optimization of coastal structures,[26] and shape optimization of aerodynamic and acoustic constraints for internal and external flows.[21]

(20) Mohammadi, B.; Pironneau, O. *Applied Shape Optimization for Fluids*; Oxford University Press: New York, 2001.
(21) Mohammadi, B.; Pironneau, O. *Annu. Rev. Fluid Mech.* **2004**, *36*, 255−279.
(22) Ivorra, B.; Hertzog, D. E.; Santiago, J. G.; Mohammadi, B. *Int. J. Numer. Methods Eng.* **2006**, *66*, 319−333.
(23) Ivorra, B.; Mohammadi, B.; Redont, P. *J. Global Optimization* **2005**, *submitted*.
(24) Mohammadi, B.; Saiac, J.-H. *Pratique de la Simulation Numerique*; Dunod, 2002.
(25) Debiane, L.; Ivorra, B.; Mohammadi, B.; Nicoud, F.; Em, A.; Poinsot, T.; Pitsch, H. *Proceeding of the Summer Program*, NASA AMES/Stanford University, 2004; pp 367−375.
(26) Isebe, D.; Mohammadi, B.; Azerad, P.; Ivorra, B.; Bouchette, F. *Proc. SIAM Math. Comput. Issues. Geosci.* **2005**.
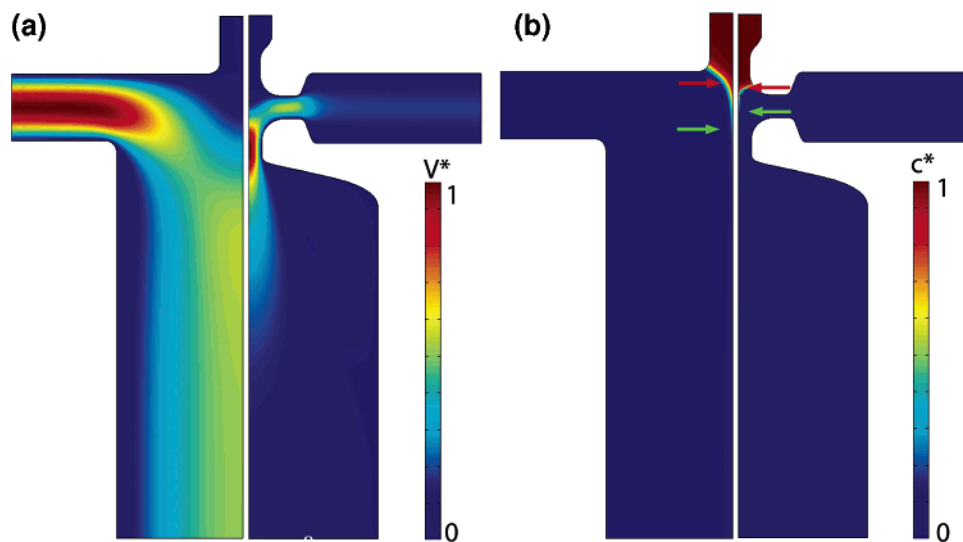
Figure 2. (a) Velocity field for the design of ref 16 (left) and the current design (right). Color indicates magnitude of normalized velocities: $V^* = (u^2 + v^2)^{1/2}/\max\{(u^2 + v^2)^{1/2}\}$. In the design of ref 16, the velocity color map is normalized by $V_{max} = 3.25$ m/s. In current design (right), the velocity color map is normalized by $V_{max} = 17.3$ m/s (b) Concentration field for design of ref 16 (left) and the current design (right). Red and green arrows point to the locations of $c = 90\%$ and $c = 30\%$ along the centerline, respectively. Color map indicates normalized concentration.

We use a global optimization algorithm, which has much less complexity than genetic algorithms to find the optimum solution. A detailed description of the algorithm is given in Ivorra et al.,[22] and we here limit our discussion to the physics of the problem, the application, and the inputs and constraints placed on the optimization. We also here discuss practically relevant sensitivity of the optimization parameters on the mixing time of the mixers.

Cost Function. For the current design, the cost function to minimize is the mixing time of a Lagrangian fluid particle traveling along the center streamline of the mixer.[16] We define the mixing time as the time for the concentration experienced by the particle to change from 90 to 30% of the initial concentration. This cost function can be expressed as

$$J \equiv t_{mix}(\hat{x}_{shape}) = \int_{x_{c=90\%}}^{x_{c=30\%}} \frac{1}{u_{\hat{x}-shape}(x)} \, dx \qquad (6)$$

where $\hat{x}_{shape}$ is the current mixer geometry, u is the velocity along the center streamline, x is the distance along the center streamline, and $x_{c=90\%}$ and $x_{c=30\%}$ are the locations where the concentration is 90 and 30% of the initial value, respectively. The 30% is chosen somewhat arbitrarily for the purpose of comparing numerical simulations to one another.

Variables: Geometry and Flow Conditions. We initiate our current SDA with our previous mixer design[16] as an initial condition. We parametrized the sharp 90° corners of our previous designs with splines to keep admissible shape regularity. The following constraints are imposed on the minimization: (1) Feature sizes (including radii of curvature) are limited to minimum of 2 μm as per the limits of the combined photolithographic and etching processes. (2) Side channels are limited to a minimum width of 3 μm to mitigate clogging issues. (3) We use physical properties of commonly used chemical denaturants and buffers for protein folding. The values for diffusivity, density, and viscosity of the simulated solutions are 2×10^{-9} m²/s, 1013 kg/m, and 10^{-3} Pa s, respectively. (4) Our numerical model is a 2D

approximation of a 3D flow field, and so we limit the local Reynolds numbers (and Dean numbers around corners) to values where the flow remains predominantly 2D. Experiments and preliminary 3D modeling show out-of-plane fluid flow and distortion of the focused stream at higher Reynolds numbers due to Dean vortex formation at the intersection of the mixer. Limiting the Reynolds and Dean numbers is effectively the same as limiting maximum outlet flow rate to $\sim 10^{-4}$ mL/s and limiting maximum channel aspect ratios (AR = width/depth) to less than unity. The constraints are similar to those of our previous optimization so that we can make meaningful comparisons between the current results and those of our previous paper.[16]

To summarize, the fixed variables in our optimization include the density, viscosity, diffusion coefficient, minimum channel width, angle of side channel entry (90°), maximum flow rate, and symmetry of the device (across vertical centerline). The overall general topology of three inlets and one outlet (with the center inlet carrying protein/denaturant solution) was also a constraint. The parameters varied are the geometry and the center-to-side channel flow rate ratio (see Ivorra et al.[1] for more details regarding the optimization). The optimized solution is "globally optimized" within these constraints. This means once the search space is set (flow rate ratio and geometry conforming to the three-inlet/one-outlet topology), the optimization code searches for the optimal solution over this space. We note that if the search space is changed, then the optimal solution may, of course, also change.

OPTIMIZATION RESULTS

The SDA optimization reduced predicted mixing time from 8 μs in the original design to 1.2 μs in the new optimized design. Figure 1 shows the geometry and mesh for the original and shape-optimized mixers. The main feature of the new geometry is a constriction of the exit channel after the intersection. The constriction results in high fluid velocities just after the intersection of the three inlet streams. Figure 2a shows the simulated velocity fields for both mixers. In the ref 16 design, the velocity along the center streamline of the exit channel is relatively small
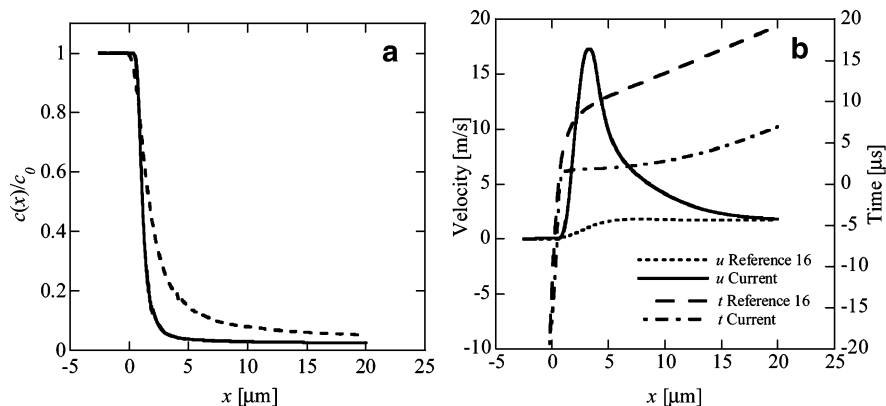
Figure 3. (a) Normalized concentration versus distance from nozzle, from simulations. Dashed line is ref 16 mixer design; solid line is current design. (b) Velocity, u, along centerline of mixer and integrated Lagrangian time, t, versus distance from nozzle. Reference 16 mixer results are shown as dotted (u) and dashed (t) lines and current results are shown as solid (u) and dash−dot (t) lines.
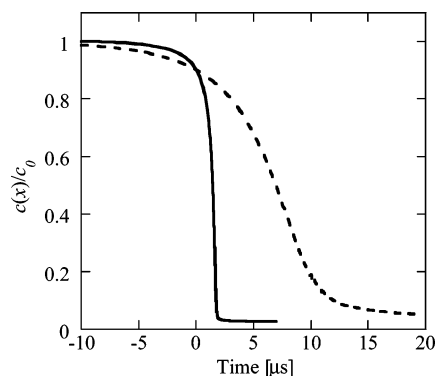

Figure 4. Predicted normalized concentration versus time. Dashed line is the mixer design of ref 16, and solid line is the current design. The older design takes 8 μs to go from 90 to 30% of the initial concentration. The current design takes only 1.2 μs.

as the convective diffusion problem develops. In contrast, the current design has a flow constriction immediately after the intersection that maintains high-velocity magnitudes and high-velocity gradients, which approximately coincide with the region where the local Lagrangian concentration drops from 90 to 30%. Figure 2b shows a detailed view of the simulated concentration fields of the two mixer designs. Superposed on each of the concentration fields are red and green arrows denoting the locations along the center line of 90 and 30% denaturant concentration, respectively. Comparison of Figure 2a and b shows how mixing occurs in approximately the same region for the old and current mixer designs, but the current mixer has ∼10-fold higher local velocities (15 m/s versus ∼2 m/s for the mixer of ref 16). The results are summarized with centerline flow profiles shown in Figure 3. Figure 3a shows the concentration along the center streamline for both mixers. The concentration drops from unity to ∼0.1 in the region $x = 0-5$ μm in both cases. In Figure 3b, we show center streamline velocity and relation between time and axial location for a Lagrangian particle. $t = 0$ is chosen at the point where the concentration reaches 90% of the initial value. The $t(x)$ curves shows clearly how the new design maintains higher absolute velocity in the mixing region.

Figure 4 shows the Lagrangian concentration (i.e., local denaturant concentration experienced by a particle traveling along the flow centerline) versus time for both mixers. These curves

are calculated by combining the concentration versus x of Figure 3a with the time versus x of Figure 3b. Again, $t = 0$ denotes the instance at which the concentration reaches 90% of the initial value. As per eq 6, the cost function is then the time at which the concentration reaches 30% of c_o. The design of ref 16 has a mixing time of ∼8 μs while the current shape-optimized design reduces this to 1.2 μs. The concentration asymptotes to a final value determined by the flow rate ratio. The process is similar to a one-dimensional transient diffusion problem with a delta initial condition.

Proteins traveling along streamlines other than the center streamline undergo a different Lagrangian concentration history. They experience different velocity and concentration fields and therefore have different mixing times. A detection volume (larger in characteristic length than the stream but much smaller than the outlet channel dimensions) along the focused stream at some $x = x_{detection}$ will sample proteins with a distribution of mixing times. We can quantify this nonuniformity of mixing times by calculating the mixing time of all the streamlines across the focused stream. We again use the mixing time definition of eq 6, but with $u(x)$ replaced by $u_{SL}(s)$, where u_{SL} represents the local fluid velocity along the streamline of interest and s represents the contour distance along the streamline. Figure 5 shows the variation of mixing times across the focused stream for the ref 16 design and the current design. We used a custom confocal microscope setup with a depth of field of approximately $\delta z = 1.5$ μm and centered at $z = 0$, so that we are only interested in streamlines in the $z = 0$ midplane of the mixer. The cross-stream coordinate, y, is nondimensionalized by the width of the focused stream, w_{fs}. The latter dimension is defined as the distance between the two streamlines separating the center and side channel flows at $x_{detection}$. $x_{detection}$ is taken at $x = 5$ μm (downstream of the nozzle exit) for this mixing uniformity analysis, at a location where the center stream velocity is uniform (less than 1% variation along the center stream from $y = -0.1$ to 0.1 μm). The term "nozzles" refers to the narrow channel sections near the intersection of the center and side channels. Streamlines originating upstream of the center nozzle and flowing near the outside wall of the center channel (these become the periphery of the focused stream) have longer mixing times than the center streamline. At the wall, the velocity is zero, so we define here the outer streamlines as those within
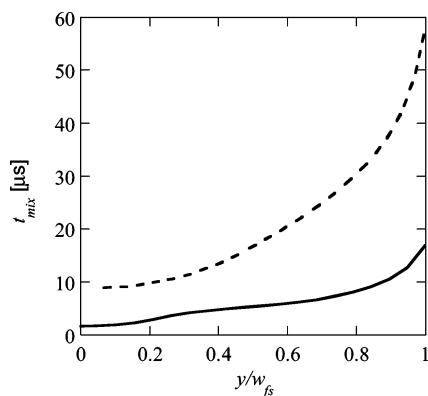
Figure 5. Predicted variations in mixing time for different streamlines in focused stream. Dashed line is the mixer design of ref 16, and the solid line is the current design. Abscissa is y coordinate at $x = -5$ μm, normalized by width of focused stream, w_{fs}. The current design demonstrates shorter and more uniform mixing times across the focused stream.

Figure 6. Bright-field reflection images of the fabricated mixers. Design of ref 16 is shown on left (a) and current shape-optimized design is shown on right (b). Focal plane is approximately coincident with the inner surface of the optical access window for each channel.

0.5 μm of the wall in the $x < 0$ μm region above the nozzle. These outer streamlines have a mixing time of 58 and 17 μs for the ref 16 and current designs, respectively. The average mixing time across the focused stream is 24.5 μs for the older design and 6.1 μs for the current design. The standard deviation of mixing times for each design is 14.7 and 3.9 μs for the ref 16 and current mixers, respectively. These results show a significant improvement in mixing time uniformity for the current optimized design over the older design.

The SDA algorithm converges in ~10 iterations, and the total number of functional evaluations is ~3600. The best element was found after 1400 evaluations. The SDA visited several attraction basins before exploring the best element basin. Each evaluation requires ~20 s on a 3-GHz Pentium computer resulting in a total computation time of 18 h. For details, see Ivorra et al.[22]

EXPERIMENTAL TECHNIQUES

Device Fabrication. We measured the mixing times of the two designs with dye-quenching experiments in silicon–glass devices to validate the numerical simulations and optimization analysis. The microfluidic mixers were fabricated on silicon substrates using contact photolithography, deep reactive ion etching (DRIE), and the channels sealed by anodic bonding of a 170-μm-thick Pyrex 7740 wafer (Sensor-Prep Services). Figure 6 shows bright-field reflection CCD camera images of the mixing regions for the ref 16 design, Figure 6a, and the current shape-optimized design, Figure 6b. The channels are 10 μm deep with vertical side walls. The lithography step limits feature sizes to ~2 μm, which imposes a physical constraint on the optimization problem. The devices have built-in filters (arrays of vertical posts with 2-μm spacing) upstream of the mixing regions to reduce clogging. The channels leading to and away from the mixing regions shown in Figure 6 are identical to those used in our previous mixer.[16]

Pressure Control and Buffer/Reagents. Solutions were pumped through the mixers with the same computer-controlled pneumatic pressure system we used for our first mixer.[16] The pressure system consists of two 0–100 psi regulators with 0.1% accuracy (Marsh-Bellofram Inc.) controlled by an analog output board (National Instrumen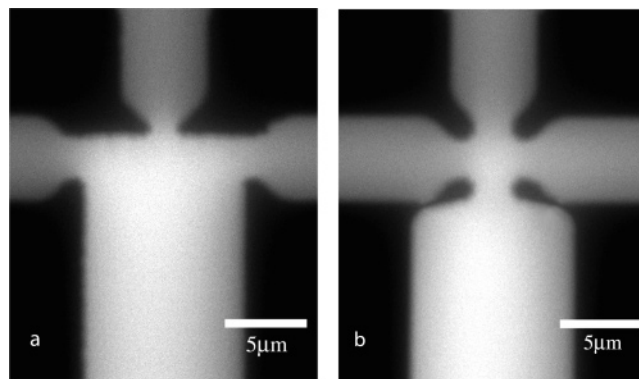ts). A custom-designed acrylic jig holds the mixer and connects it via O-rings to fluid reservoirs where the pneumatic lines interface to create a pressure head. The two regulators allow precise and independent control of flow rates in the center and side channels. We used a dye solution of 2 MDa dextran-conjugated fluorescein at 10 μM (Molecular Probes), diluted in 100 mM phosphate-buffered saline (PBS; Sigma-Aldrich) for the dye-quenching experiments. This dye solution was mixed with either 500 mM potassium iodide prepared in 100 mM PBS for quenching or pure buffer (100 mM PBS) for unquenched mixing. All solutions were filtered with 0.1-μm syringe-driven filters (Millipore Inc.) prior to use.

Experimental Setup. We obtained two image scans with exposure times of 3.9 ms/pixel for each experiment to obtain the intensity ratio for dye quenching: one image with a dye center stream mixing into buffered salt solution sheath streams (quenched intensity, I_{quenched}) and one image with the dye mixing into buffer solutions (unquenched intensity, $I_{\text{unquenched}}$). The intensity ratio is obtained from these two images, RI = $I_{\text{quenched}}/I_{\text{unquenched}}$. Registration of the two images is achieved by aligning notches etched into the side walls of the center inlet 10 μm upstream of the intersection (not shown).

Confocal Optical System. Experiments were performed on a custom-built confocal microscope. An argon ion laser (Coherent Inc.) provided excitation at 488 nm through a 488-nm notch filter and a 100× 1.4 NA objective (Nikon). Fluorescence emission was collected with the same objective, passed through a dichroic mirror, 50-μm pinhole (Newport Co.), and a 500-nm long-pass filter and detected with an avalanche photodiode (Perkin-Elmer Inc.). Images were integrated by scanning with a three-axis piezoscanning stage (Physik Instrumente) controlled with a commercial scanning controller and software (Veeco Instruments Inc.). Typical x–y scans were 7.5 μm wide and 60 μm long with 0.1-μm resolution and taken at the vertical midpoint of the channels where the flow is approximately two-dimensional.

Fluorescence Quenching. Typical mixer characterization techniques to determine mixing times use the quenching of a slowly diffusing fluorescent dye mixed with a buffer containing a fast-diffusing quencher.[27,28] This approach decouples the kinetics

(27) Kamholz, A. E.; Weigl, B. H.; Finlayson, B. A.; Yager, P. *Anal. Chem.* **1999**, *71*, 5340−5347.
(28) Oddy, M. H.; Santiago, J. G.; Mikkelsen, J. C. *Anal. Chem.* **2001**, *73*, 5822−5832.
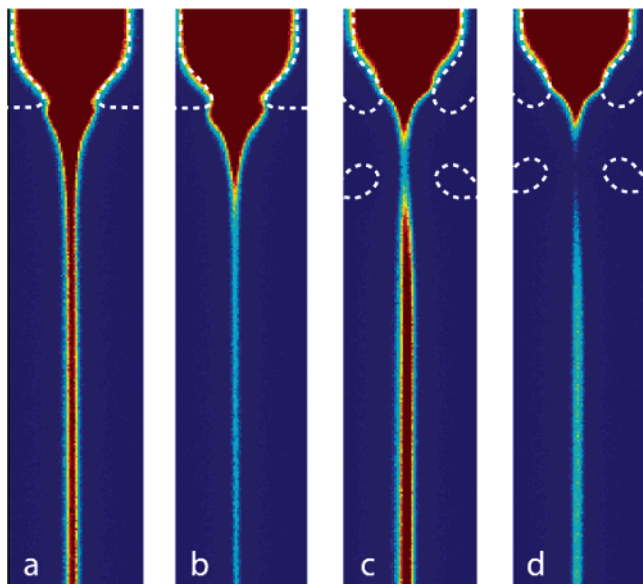
Figure 7. Confocal images from dye-quenching experiments. Flow is from top to bottom and false color map indicates fluorescence intensity (red is high intensity from fluorescein, and blue is low intensity). Dashed lines show approximate wall locations. Scans are approximately 4 μm wide and 40 μm tall. (a) Mixer design of ref 16 with buffer only in side channels—no quenching is present. (b) Reference 16 design with 500 mM potassium iodide in side channels—fluorescein is quenched. (c) Current mixer design with buffer in side channels, and (d) current design with potassium iodide in side channels.

associated with the diffusion of the dye from those of the quencher. To compare the mixing times of our original and shape-optimized designs, we quench a high molecular weight fluorescent dye (10 μM fluorescein conjugated with dextran) with iodide ions from a 500 mM potassium iodide solution. Iodide ions reduce the quantum yield of the dye molecules through collisional quenching, and the resulting decrease in intensity is used to measure the local concentration of iodide.[29]

The ratio of intensities of quenched dye solutions to unquenched solutions (RI) were calibrated with salt concentration using a spectrofluorometer in a preliminary calibration study in which reactants were in chemical equilibrium. The empirical transform between RI and salt concentration is shown in Figure S-1 (Supporting Information). This curve was obtained from equilibrium measurements using the spectrofluorometer. At concentrations near 500 mM, dye intensity is reduced to ~25%.

EXPERIMENTAL RESULTS

Confocal Images. Figure 7 shows typical scanned confocal images from dye-quenching experiments in the ref 16 (a, b) and current (c, d) mixer designs. As expected, the fluorescence intensity of the unquenched streams (a, c) are higher than that of the quenched streams (b, d). Note that the velocity field is the same between the quenched and unquenched images of a given geometry, even though the intensity field is different. The concentration of dye molecules is also the same between the quenched and unquenched cases. Fluorescence intensity is, of

(29) Lakowicz, J. R. *Principles of Fluorescence Spectroscopy*, 2nd ed.; Kluwer Academic/Plenum Publishers: New York, 1999.

course, reduced in the quenched experiments due to the presence of iodide ions. The shape-optimized mixer shows a dip in fluorescent intensity in the narrow "neck" region for both the unquenched and quenched dye experiments. This inflection in centerline intensity is an artifact of the imaging procedure. The vertical aspect ratio for the "neck" region is low enough (AR = 1/5) such that the opaque silicon channel side walls partially block the paths of light of excitation and emission. This artifact, however, does not affect our quantification of quenching rate as our measurements are based on unquenched-to-quenched intensity ratios and not on the absolute values of intensity.

Both mixer designs showed typical hydrodynamic focusing of the dye solution into a thin stream. The shape-optimized design improved mixing time by increasing velocity gradients in the region of highest concentration gradients. The higher velocity gradients in the focusing region of the optimized design more quickly stretch the interfaces between the center stream and the sheath streams. This reduces the time Lagrangian particles reside in the two-dimensional convective diffusion region of the early phase mixing and more quickly achieves the "focused stream" state where mixing time is limited mostly by spanwise (y-direction) diffusion.

Data Analysis and Calibration. We normalized images by subtracting background images of unseeded buffer flow, and the quenched and unquenched scans were aligned in x, y, and θ (rotation). We extracted intensity versus x profiles by averaging $\Delta y = 0.5$-μm-wide strips at $\Delta x = 0.1$ μm spacing along the focused stream. The ratio of intensity of the quenched image to unquenched image, RI = $I_{quenched}/I_{unquenched}$, is shown in Figure 8a for both mixer designs. For $x < 0$, the dye and salt solution are not yet in contact and there is no quenching. After the two streams intersect, iodide ions begin to diffuse into the dye stream and RI rapidly decreases to 35% of its initial value at $x = 5$ μm (RI drops to ~25% at $x = 25$ μm, as expected from the equilibrium measurements). We used simple linear interpolations of the transform data to convert the raw RI data of Figure 8a to the concentration data of Figure 8b. We used the same calibration method for all experiments.

Lagrangian Time History. Next, we want to estimate the concentration versus time history that a Lagrangian particle would experience given our measurements of the Eulerian concentration field and our predictions of Eulerian velocity field. The Eulerian frame of reference is stationary with respect to the device. In the Eulerian description, a steady-state velocity field is used that defines fluid velocity at all points within the fluid (this vector field is thus a function only of space). In a Lagrangian frame of reference, we describe the velocity vector of an identifiable fluid particle as it travels through space (this vector quantity is thus only a function of time). In the latter frame, fluid velocities and concentrations change in time as the fluid element and frame of reference moves through gradients of the Eulerian field. The numerical models solve for the Eulerian velocity and concentration fields, but it is more appropriate to describe the mixer performance in terms of the conditions that a protein would experience as it flows through the mixer (a Lagrangian frame of reference). To this end, we first integrate the function $1/u(x)$ along the focused stream centerline using the numerical velocity field prediction (see the form of eq 6). This conversion from the spatial coordinate, x,

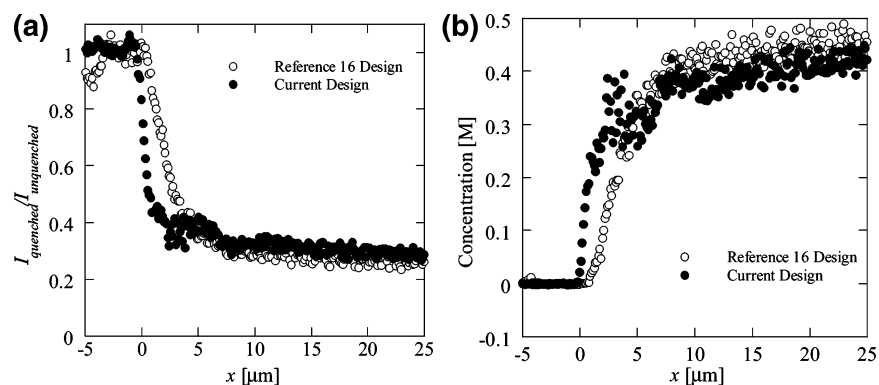**Figure 8.** (a) Intensity ratio versus distance from nozzle from experiments shown in Figure 7. Intensity ratio = $I_{quenched}/I_{unquenched}$. Open circles are data from the mixer design of ref 16; closed circles are data from the current design. (b) Concentration of potassium iodide versus distance from nozzle (same experiment as Figure 7). Open circles are ref 16 design; closed circles are the current design.
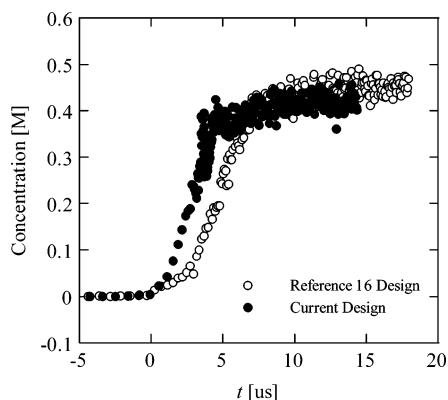

Figure 9. Potassium iodide concentration versus time. The current mixer optimization improved the mixing time by ~3 μs over the design of ref 16. Open circles are ref 16 design, and closed circles are current design.

Table 1. Numerical Parameter Sensitivities[a]

parameter	t_{mix} (μs)	% change
Flow Rate		
center channel +10%	0.8	−33
center channel −10%	2.1	+75
side channel +10%	1.2	0
side channel −10%	0.8	−33
ratio center/side +25%	1.2	0
ratio center/side −25%	2.3	+92
Geometry		
exit channel width +1 μm	1.2	0
exit channel width −1 μm	1.2	0
side channel width +1 μm	1.0	−17
side channel width −1 μm	1.1	−8
center channel width +1 μm	12.2	+900
center channel width −1 μm	8.3	+600

[a] Note: decreases in mixing time from the optimum found in this paper result from violations of the constraints imposed on the current problem.

to a Lagrangian time coordinate, t was given as Figure 3b. We can then map the parametrized Lagrangian time function $t(x)$ onto the streamwise distance for the measured potassium iodide concentration field (which was determined directly from RI with equilibrium measurements from the spectrofluorometer, Figure S-1). Figure 9 shows the concentration of KI versus (Lagrangian particle) time for both the original mixer design (open circles) and the shape-optimized design (closed triangles). The shape optimization reduces mixing time from 7 μs in the ref 16 design to ~4 μs in the current design. As we discuss below, the performance of the new mixer matches predictions within our experimental uncertainty.

Experimental Uncertainty. The discrepancies between the simulated and the measured mixing times for the ref 16 and current mixers (predicted 8 μs versus the measured 7 μs for the old, and predicted 1.2 μs versus the measured 4 μs for the current) may result from several sources of uncertainty: (1) The fabricated geometry was different than the geometry suggested by the optimization; (2) there are uncertainties in the applied pressures and flow rates; (3) the finite length of the diffraction spot resulting from the confocal imaging limits measurement resolution; (4) image noise in the detection system; (5) errors associated with the conversion from quenching ratio to salt concentration; and (6) the two-dimensional numerical models are only approximations to the full three-dimensional flow fields. We used our simulations and estimates of the performance of our imaging system to explore

the relative importance of each of these factors. Table 1 lists the sensitivity of the modeled mixing time to various channel dimensions and flow rates. By analyzing microscopy images such as those shown in Figure 6, we found feature sizes and feature locations of the fabricated geometry were within ~±0.5 μm of the modeled geometry. Typically the fabricated device had slightly larger channel and nozzle widths than the model. These differences are mostly a result of the lithography step of fabrication. As shown in Table 1, the mixing time is most sensitive to the width of the center inlet channel. A ±0.5-μm change in center channel width increases mixing time by a factor of ~4 (a ±1-μm error results in a mixing time increase of ~6−9-fold). The strong sensitivity of mixing time on center channel width implies that the focusing region (where the center channel enters the intersection to the point downstream where the focused stream width stops changing) largely determines the mixing time. Narrower center nozzles (with appropriate changes in the flow rate ratio) can typically achieve shorter mixing times; however, clogging issues and the resolution of the photolithography in practice limit how small these center nozzles can be made. One important lesson we may draw from the current design is that, for the same center nozzle width, the width of the side channel nozzles can also have a significant effect on mixing time.

We estimate our flow control system supplies source pressures with 0.1% full-scale accuracy. As shown in Table 1, even changes

in flow rates of up to ±10% do not change the mixing time by more than 100%, so that significant deviations in measured mixing time due to applied pressure variations are unlikely. We also estimated the sensitivity of flow rates to applied pressures using analytical models for flow in the supply channels. For these calculations, we used channel widths measured from optical and scanning electron microscope images. We measured channel depths with a profilometer prior to bonding the glass coverslip (we measured depth variations of $\sim\pm0.5$ μm from the etching process). The uncertainty in channel dimensions results in an uncertainty in the analytical flow rate calculations of $\sim\pm9\%$, and an uncertainty in the flow rate ratio of $\sim\pm0.5\%$. Again, such flow rate ratio errors result in mixing time changes of less than 100%.

Noise in the detection system (due to the photodiode, counting hardware, stray light, etc.) and the conversion from intensity ratio to salt concentration will introduce uncertainty in the mixing time measurement. We estimated this uncertainty by measuring the standard deviation of the time data (see Figure 9) as the concentration reaches a steady value (chosen as 0.4 M here). The optimized mixer has a mixing time standard deviation of 0.28 μs as the concentration reaches 0.4 M, and so we conclude that the effects of random measurement noise on (the time averaged) mixing time are negligible.

Our confocal detection system uses diffraction-limited optics with a confocal spot size estimated at 0.5 μm. Scanned images of dye intensity are therefore essentially low-pass filtered via convolution with a Gaussian kernel. As shown in Figure 3a, we expected high concentration gradients in the region within ~2 μm of the nozzle exit, particularly in the case of the optimized mixer. The finite spatial resolution of the confocal detection system will tend to smooth these sharp gradients resulting in artificially longer measured mixing times. We can estimate the error in measured mixing time due the confocal spot size by approximating the imaging as a convolution between the simulated concentration field with a 0.5-μm wide Gaussian kernel. This optical convolution alone increases the estimate of mixing time from 1.2 to 6.1 μs.

CONCLUSIONS

We have applied a shape optimization method to the design of fast microfluidic mixers and to reduce mixing time. The optimization combines a semideterministic algorithm and numerical simulations to minimize the mixing time by varying the mixer geometry and flow conditions within a specified set of constraints. The optimization reduced the expected mixing time from 8 μs in the previous mixer design to 1.2 μs in the shape-optimized design. This mixing time improvement was achieved solely by varying geometry and flow rates of the mixer within the minimum feature size and maximum flow rate constraints.

The mixers were fabricated in silicon (DRIE etched 10 μm deep) and anodically sealed with a glass coverslip. The photolithography step constrains the minimum feature size to ~2 μm. We experimentally measured mixing time with a dye-quenching assay. High molecular weight fluorescein was quenched with salt ions to measure diffusion of the salt ions in the mixers. We measured a reduction in mixing time from 7 μs in the previous mixer design to 4 μs in the current shape-optimized design. The measured mixing times fall within the estimated experimental uncertainty (a few microseconds) of the predicted mixing time.

One of the major barriers to reducing the mixing time further is the appearance of three-dimensional flows at higher Reynolds number, which make the flow field difficult to model. Dean's vortices begin to develop in the mixing region at higher flow rates. We are currently working to solve this problem by building full three-dimensional numerical models as well as developing new geometries that produce less curvature in the velocity field. Note that 2.3× and 3.9× reductions in mixing time are possible by enabling an increase of the flow rates by 2× and 10×, respectively.

The minimum resolution of our lithography process also limits the mixing time The numerical simulations indicate that 2× and 10× reductions in channel widths should reduce the mixing time by 1.8× and 8.1×, respectively. Two potential ways of reducing minimum feature size include using a reducing projection aligner or direct writing with an e-beam to achieve submicrometer lithographic features in the photoresist. Increasing flow rates and reducing nozzle widths, however, both make clogging an even more important issue. Our mixers have on-chip integrated filters to reduce clogging of the intersection, and the improvements mentioned above would require more care in filtering solutions and fabricating clean devices. Mixer operation (not just fabrication and loading) in a clean environment may be beneficial.

We have used these mixers to measure the folding kinetics of a benchmark protein ACBP[16] using Forster resonance energy transfer, and are currently using them to study protein collapse of a variety of proteins including CI2 and protein L.[30] We have also fabricated these mixers with fused-silica substrates[31] and are measuring folding of unlabeled proteins such as cytochrome c, lysozome, and apomyoglobin with UV−visible spectroscopy.

SUPPORTING INFORMATION AVAILABLE

Figure S-1, a calibration plot of fluorescence intensity ratio versus salt concentration from equilibrium spectrofluorometer measurements. This material is available free of charge via the Internet at http://pubs.acs.org.

(30) Xavier, M.; Jager, M.; Hertzog, D. E.; Santiago, J. G.; Bakajin, O.; Weiss, S. *49th Annual Meeting of the Biophysical Society*, Long Beach, CA, February 12−16, 2005.

(31) Hertzog, D. E.; Santiago, J. G.; Bakajin, O. *Eight International Conference on Micro Total Analysis Systems*, Malmo, Sweden, September 2004.